Journal of CO2 Utilization 50 (2021) 101588

Contents lists available at ScienceDirect

Journal of CO2 Utilization

journal homepage: www.elsevier.com/locate/jcou

Comparative study of CO_2 photoreduction using different conformations of CuO photocatalyst: Powder, coating on mesh and thin film

Manuel Alejandro Ávila-López [a,1], Stelios Gavrielides [b,1], XiaoJiao Luo [b,1], Abah Ezra Ojoajogwu [b], Jeannie Z.Y. Tan [b,*], E. Luévano-Hipólito [a,c,*], Leticia M. Torres-Martínez [a,*], M. Mercedes Maroto-Valer [b,*]

[a] Universidad Autónoma de Nuevo León, Facultad de Ingeniería Civil-Departamento de Ecomateriales y Energía, Cd. Universitaria, C.P. 66455, San Nicolás de los Garza, NL, Mexico

[b] Research Centre of Carbon Solutions (RCCS), School of Engineering & Physical Sciences, Heriot-Watt University, Edinburgh, United Kingdom

[c] CONACYT- Universidad Autónoma de Nuevo León, Facultad de Ingeniería Civil-Departamento de Ecomateriales y Energía, Cd. Universitaria, C.P. 66455, San Nicolás de los Garza, NL, Mexico

ARTICLE INFO

Keywords:
Photocatalysis
Thin film
CuO
Powders
Solar fuels

ABSTRACT

The use of CuO-based photocatalysts for CO_2 photoreduction has been extensively reported in the literature. However, the comparison of the photocatalytic activity and selectivity from the published results becomes difficult due to different experimental conditions (*i.e.*, synthesis method, configuration of photocatalyst, flow rate of gas, water content, light intensity) and reactor geometry employed. Hence, in this work different conformations of CuO-based photocatalyst, namely powder (*i.e.*, synthesized using precipitation, sonochemical and hydrothermal-microwave treatment), coating on glass fiber mesh, and thin film, were tested using the same photoreactor and experimental conditions. All CuO photocatalysts exhibited 100 % product selectivity towards CH_4 over CO and the CuO coating on the glass fiber mesh exhibited the highest production of CH_4 (56.3 μmol g_{cat}^{-1} h^{-1}). The morphology, particle size, particle dispersity, and presence of impurities/defects within the CuO photocatalysts had a significant effect on photocatalytic activity. A numerical model, which was built using COMSOL, revealed that the experimental data obtained in this simulated photocatalytic activity study fitted well, however, further optimization was needed.

1. Introduction

CO_2 is the most abundant anthropogenic greenhouse gas responsible for global warming [1,2]. Various mitigation approaches have been proposed to decrease CO_2 emissions, including CO_2 conversion and utilization (CCU) [3–5]. Solar energy to drive the photoreduction of CO_2 into chemicals and fuels provides an interesting approach for the production of syngas (CO and H_2), CH_3OH, CH_4, HCOOH and HCOH amongst others [6–12].

Photocatalyst requirements, including a high affinity towards CO_2, rapid adsorption/desorption kinetics, high thermal and mechanical stability and high specific surface area with active sites, have been proposed to enhance the photocatalytic conversion of CO_2 into value-added products [13]. In view of this, transition metal oxides represent an excellent option since they can desorb the adsorbed gas at a relatively low temperature (<200 °C) compared to alkali metals and alkaline metal oxides [13]. In addition, they are non-toxic and abundantly available. Among the transition metal oxides, copper-based metal oxides (*i.e.*, Cu_2O, CuO, Cu metal) are the most widely reported materials for CO_2 photoreduction [14,15]. This is because CuO possesses the highest electronegativity and highest number of basic sites for CO_2 adsorption and a more favorable CO_2 adsorption capability (ΔH= -45 kJ mol^{-1}) compared to other transition metal oxides [16,17].

Many studies have demonstrated the use of CuO as photocatalyst for CO_2 reduction [8,18–23], as summarized in Table S1. However, the comparison of the results from the literature is challenging due to different synthesis approaches, experimental conditions, and geometry of photoreactor employed. Hence, in this study, the comparison of CuO

* Corresponding authors.
E-mail addresses: j.tan@hw.ac.uk (J.Z.Y. Tan), edith.luevanohp@uanl.edu.mx (E. Luévano-Hipólito), lettorresg@yahoo.com (L.M. Torres-Martínez), m.maroto-valer@hw.ac.uk (M.M. Maroto-Valer).
[1] These authors contributed equally.

https://doi.org/10.1016/j.jcou.2021.101588
Received 4 March 2021; Received in revised form 17 May 2021; Accepted 24 May 2021
Available online 1 June 2021

photocatalyst in different conformations (*i.e.,* powder, thin film, and coatings on glass fiber mesh) is investigated under the same experimental conditions. Moreover, three commonly used synthesis methods, including precipitation, sonochemical, and microwave synthesis are employed to fabricate powder samples.

In addition to the development of photocatalysts for CO_2 photoreduction, significant work has been devoted to developing advanced photoreactors in an attempt to improve the current very low conversions [24,25]. To address these engineering challenges, a validated Multiphysics model for CO_2 photoreduction under UV–vis light irradiation was developed herein. The model developed was coupled with computation fluid dynamics, mass transport, reaction kinetic and light transport in a continuous flow reactor. Three essential factors (*e.g.*, CO_2 flow rate, inlet H_2O mole fraction and light intensity) in the CO_2 photoreduction were simulated. This numerical modelling is also expected to improve our understanding of the CO_2 photoreduction mechanism, and thereby, provide a useful tool to optimize the reaction process.

2. Experimental

2.1. Material synthesis

2.1.1. Powder

2.1.1.1. Precipitation method. 5.98 g of $Cu(CH_3COO)_2{\cdot}H_2O$ (Fermont, 99 %) was dissolved in 40 ml of deionized water (DI). Then, 10 ml of 0.6 M of NaOH (Fermont, 99 %) was added dropwise into the solution. The solution was then heated for 3 h at 80 °C under vigorous stirring. The dark brown precipitate was washed with sufficient DI water, to remove all the possible residual precursor. The collected powder was dried in the oven at 80 °C overnight and the sample obtained was denoted as CuO P.

2.1.1.2. Sonochemical method. The CuO powder sample was synthesized following a procedure reported previously [26]. Briefly, 0.38 M of $Cu(CH_3COO)_2{\cdot}H_2O$ solution was dissolved in DI water. Then, 0.6 M of NaOH was added dropwise into the first solution with vigorous stirring at 50 °C. The resulted solution was exposed to sonochemical energy for 25 min using an equipment Hielscher's UP200Ht at 100 W, with capacitance and an amperage of 50 and 20%, respectively. After the sonication treatment, the resulted brown suspension was washed with DI water for three times. Finally, the dark brown powder obtained, which denoted as CuO US, was dried in the oven at 80 °C overnight.

2.1.1.3. Microwave-hydrothermal method. An aqueous solution of 0.6 M of $Cu(CH_3COO)_2{\cdot}H_2O$ was prepared under vigorous stirring for 30 min. Then, 0.6 M of NaOH was added dropwise. After that, the mixture was treated in a microwave reactor (Mars 6) at 80 °C with 300 W for 60 min. The resulted precipitate was washed with DI water and centrifuged a few times until the water was clear. Finally, the powder obtained was dried at 80 °C for 12 h and the resultant sample was denoted as CuO MW.

2.1.2. Coating

A glass fiber mesh with a grit slit of 2.7 nm was used as the substrate for CuO coating fabrication. Firstly, the glass fiber substrate was cleaned with acetone, methanol, and then DI water under sonication for 20 min and then dried at 80 °C overnight. Then, the cleaned glass fiber mesh substrates were placed in an autoclave that was filled with 0.06 M of $Cu(CH_3COO)_2{\cdot}H_2O$ solution. After that, 0.6 M of NaOH was added dropwise into the solution under vigorous stirring. Next, the autoclave was placed in the microwave reactor at 80 °C with 300 W for 60 min. The resulting brown coating on the glass fiber mesh was washed with DI water and centrifuged a few times until the water was clear and then dried at 80 °C overnight and the sample denoted as CuO Coat.

2.1.3. Thin film

Fluorine-doped tin oxide (FTO) TEC-15 glass was purchased from Ossila (2.5cm × 2.5cm, roughness of 12.5 nm, FTO layer thickness of 200 nm, 83.5 % transmission and resistivity of 12–14 Ω cm^{-1}). The FTO substrate was cleaned before use with a mixture of isopropanol, water, and acetone with a 1:1:1 ratio. The FTO glass was submerged into the solution and placed in a sonication bath for 1 h. The FTO glass was then removed and dried in air for 30 min at 75 °C on a hot plate.

Copper (II) acetate (Aldrich, 98 %) solution was prepared using 2.742 g in 50 ml of ethanol, forming solution A. Then, solution A was stirred for 30 min. After that, 12 µl of diethanolamine ($C_4H_{11}NO_2$, Aldrich ≥98 %) and 25 µg of ethylene glycol ($C_2H_6O_2$, Alfa Aesar ≥99 %) were added into solution A and stirred for 30 and 60 min, respectively, obtaining solution B that was used to fabricate CuO thin film using a spin coater (Model P6700). Solution B was added drop by drop onto a cleaned FTO glass, which was placed on the sample stage of the spin coater spinning at 3000 rpm. After that, the FTO coated was dried in air at 100 °C for 10 min and then calcined at 400 °C (ramp rate: 10 °C min^{-1}) for 1 h, with the resulting sample labelled as CuO TF.

2.2. Characterization

The samples morphology was analyzed using Scanning Electron Microscopy (SEM, JEOL 6490). To investigate the crystallinity and phase identification, X-ray diffraction (XRD) patterns were obtained using a Bruker D8 Advanced Diffractometer equipped with Cu Kα radiation (λ=1.5418 Å) and compared with the ICDD-JCPDS powder diffraction file database; and Raman spectra were collected using a Renishaw *inVia* Raman Microscope with 785 nm excitation source. Diffuse reflectance of all the samples was measured using a Perkin Elmer Lambda 950 UV–vis equipped with an integrating sphere (150 mm). X-ray photoelectron spectrum (XPS) analysis were performed using a Thermo Fisher Scientific NEXSA spectrometer. The samples were analysed using a micro-focused monochromatic Al X-ray source (19.2 W) over an area of approximately 100 microns. Data were recorded at pass energies of 200 eV for survey scans and 50 eV for high resolution scan with 1 eV and 0.1 eV step sizes, respectively. Charge neutralisation of the sample was achieved using a combination of both low energy electrons and argon ions. C 1s electron at 284.8 eV was used as standard reference to calibrate the photoelectron energy shift. All the data analysis was performed on the CasaXPS software (version: 2.3.20rev1.0). Fourier Transform Infrared spectroscopy (FTIR), which was performed on Thermo Nicolet iS50 (1000−4000 cm^{-1}), was used to characterize the surface of the materials. *Operando* Diffuse Reflectance Infrared Fourier Transform Spectroscopy (DRIFTS) experiments were conducted on Agilent Cary 600 series spectrometer equipped with Harrick Praying Mantis reaction cell. The gas inlet of the cell was directly connected to a flow system equipped with mass flow controllers and a temperature controller. The cell outlet was connected to the mass spectrometer Hiden QGA MS. In each experiment, 20 mg of crushed powder was placed in the cell. Before reaction, the KBr background was collected in presence of CO_2 which was flowing through bubbler. 64 scans were collected per spectrum with a spectral resolution of 4 cm^{-1} and in the spectral range of 400−4000 cm^{-1}. The experiment was performed under UV–vis irradiation at 24 and 40 °C and dark (24 °C) conditions to simulate the experimental conditions within the photocatalytic reactor.

2.3. CO_2 photoreduction tests

The CO_2 photocatalytic reduction tests were performed under UV–vis light irradiation using the experimental set-up and procedure as described in the authors published work [27]. Briefly, the sample was loaded in the middle of the photoreactor. To purge the system, three repetitive steps of placing the system under vacuum to -1 bar and the vacuum released with CO_2 (99.995 %) to 1 bar were performed. The CO_2 was then released through the injection port of the gas chromatograph

(GC, Agilent, Model 7890B series), leaving a positive pressure of 0.2 bar, before the system was sealed and placed under vacuum overnight before each measurement. The flow rate of CO_2 was set to 0.35 ml min^{-1} and passed through the temperature controlled (±0.1 °C) aluminium body saturator for at least 16 h to allow the system to equilibrate. Relative humidity (±1.8 % RH) was measured using an inline Sensirion SHT75 humidity sensor potted (MG Chemicals 832HD) into a Swagelok 1/4″ T-piece. The temperature of the photoreactor (40 °C) was controlled using a hotplate and the surface of the coated photocatalyst measured using a Radley's pyrometer (±2.0 °C). An OmniCure S2000 with 300−600 nm wavelength was used as the light source was placed 30 mm above the surface of the investigated sample. Irradiance (150 $mWcm^{-2}$) at the exit of the fiber optic light guide was measured before each experiment using an OmniCure R2000 radiometer (±5%). An inline GC) with a Hayesep Q column (1.5 m), 1/16 inch OD, 1 mm OD), Molecular Sieve 13X (1.2 m), 1/16-inch OD, 1 mm ID), thermal conductivity detector (TCD), nickel catalyzed methanizer and flame ionization detector (FID) was used to analyze the output of the photoreactor every four minutes. The GC was calibrated using 1000 ppm calibration gas (H_2, CO, O_2 and CH_4) in a balance of Ar gas) that was further diluted with Ar (99.995 %) using mass flow controllers to 17.04, 4.62 and 1 ppm using the FID detector for CH_4 and CO, respectively, and 69.49, 34.72 and 17.04 ppm using the TCD detector for H_2 and O_2.

The CO_2 utilization rate was determined by taking the molar percentage of CO_2 inlet: CO_2 outlet as the amount of CO_2 consumed. The cycling test (*i.e.*, 3 runs) was performed using the optimized sample, which was cleaned with DI water and dried on a hotplate at 100 °C for 2 h before each run.

The quantum yield (ϕ) was measured under similar photocatalytic reaction conditions using the same light source (OmniCure S2000 with 300−600 nm wavelength). The incident flux was determined by a Laboratory Spectroradiometer (Apogee Instruments). The ϕ values of CH_4 evolution for the CO_2 photoreduction reaction were calculated according to the following equation:

$$\phi CH4\,(300-600\,\mathrm{nm}) = \frac{amount\ of\ product\ formed}{amount\ of\ photons\ adsorbed\ in\ the\ range\ of\ 300-600\,nm}$$

2.4. Simulation studies

COMSOL Multiphysics version 5.3 was used to solve the numerical equations and develop a stationary numerical model for CO_2 photoreduction. The model built was validated with the experimental data obtained in this study. A three-dimensional continuous flow reactor was simulated. The following general assumptions were made: (1) steady state laminar flow of incompressible Newtonian fluid with constant physical properties; (2) all gases were assumed as ideal gases; and (3) the whole reactor was assumed isothermal with temperature of 298 K, which means the Arrhenius expressions were ignored in the model. To assure the accuracy of the solutions obtained, a grid independence check was conducted. The computational domain of the 3D models developed for samples CuO MW, CuO Coat and CuO TF were mainly discretized with tetrahedral, prism and triangular elements. Direct solution procedure was conducted by using the Multifrontal Massively Parallel Solver. The abbreviations and symbols used are listed in Table S2 and a summary of all parameters used are presented in Table S3.

2.4.1. Hydrodynamics and mass transfer

The physiochemical behavior is described by using the coupled continuity equation, Navier-Stokers equations with Darcy's term as shown in Eq. (1):

$$\nabla\rho\frac{\partial u}{\partial t} + \rho u\nabla u = -\nabla p + \nabla\left[\mu\left(\nabla u + (\nabla u)^T\right) - \frac{2}{3}\mu\nabla u\right] - \frac{\varepsilon\mu u}{k} \quad (1)$$

where p denotes as pressure, ρ and u denote the density of gas and velocity vector, respectively.

In the CFD model, mass transport of gas species is calculated by extended Fick's law as shown in Eq. (2):

$$N_j = -\frac{1}{RT}\left(\frac{K_0 y_j P}{\mu}\nabla P - D_j^{eff}\nabla\left(y_j P\right)\right) \quad (2)$$

Here, μ is the gas viscosity, K_0 is the permeability, y_j and D_j^{eff} are the mole fraction and effective diffusivity of species j, respectively.

D_j^{eff} is the effective diffusion coefficient for species j corrected using the Bruggeman relationship, as shown in Eq. (3):

$$D_j^{eff} = \frac{\varepsilon_m}{\tau_m}D_j \quad (3)$$

where ε_m, τ_m is the porosity and tortuosity, respectively, whereas D_j is the diffusion coefficient which composed of mass-average Stefan-Maxwell diffusivity, D_j^m, and Knudsen diffusivity D_j^K as shown in Eq. (4),

$$D_j = \left(\frac{1}{D_j^m} + \frac{1}{D_j^K}\right)^{-1} \quad (4)$$

2.4.2. Photochemical reaction

The kinetic model is shown in Eq. (5):

$$CO_2 + 2H_2O \rightarrow CH_4 + 2O_2$$

$$R = kI^{\alpha}\left(\frac{K_{H_2O}P_{H_2O}K_{CO_2}P_{CO_2}}{\left(1 + K_{H_2O}P_{H_2O} + K_{CO_2}P_{CO_2}\right)^2}\right) \quad (5)$$

where, k is the reaction rate constant, I represents the light intensity and α is reaction order. K_{H_2O} and K_{CO_2} are the constants for adsorption and desorption of H_2O and CO_2, respectively. Related kinetic parameters are listed in supplementary Table S2.

3. Results and discussion

3.1. Crystal phase

The powder samples synthesized using different approaches (*i.e.*, precipitation, ultrasonication and microwave synthesis) exhibited the monoclinic phase of CuO (JCPDS: 45−0937, Fig. 1a–c). The peaks at 32.5, 35.8 and 38.6° corresponded to the (110), (-111) and (111) planes, respectively. The most intense peak at 2θ = 38.6° was used to estimate the crystallite size of the samples, which was 10−12 nm.

The crystal phase of CuO Coat also exhibited monoclinic phase (JCPDS: 45−0937, Fig. 1d). However, the signal-to-noise of the XRD pattern in CuO Coat was much lower than that for CuO P, CuO US and CuO MW due to the low thickness of the coating on the glass fiber mesh. The XRD pattern of sample CuO TF (Fig. 1f) only revealed a strong diffraction at 2θ = 37°, corresponding to the FTO conductive thin film (Fig. 1e). This was due to the overshadow of the diffraction pattern of the conductive thin film. Hence, Raman spectroscopy, which is much more sensitive towards the vibration of the crystal lattice, was employed [28]. Three bands centered at 287, 341, and 615 cm^{-1}, which were attributed to A_g, B_{1g}, and, B_{2g} modes of CuO, respectively, were observed in samples CuO TF (Figure S1a) [29–32]. However, these CuO peaks were broadened and slightly red-shifted, attributing to different sizes of the CuO particles (further discussed in the next section) [30]. Sample CuO Coat also exhibited CuO characteristic bands. Additional bands, including PO_4^{3-} (ν1) (960 cm^{-1}), [33] Si-*N*-Si (870 cm^{-1}), vibration outside the plane C–H (760 cm^{-1}), deformation outside the ring C–H (690 cm^{-1}) [34], P—O—P (620 cm^{-1}) were identified originated from the glass fiber mesh substrate (Figure S1b and c).

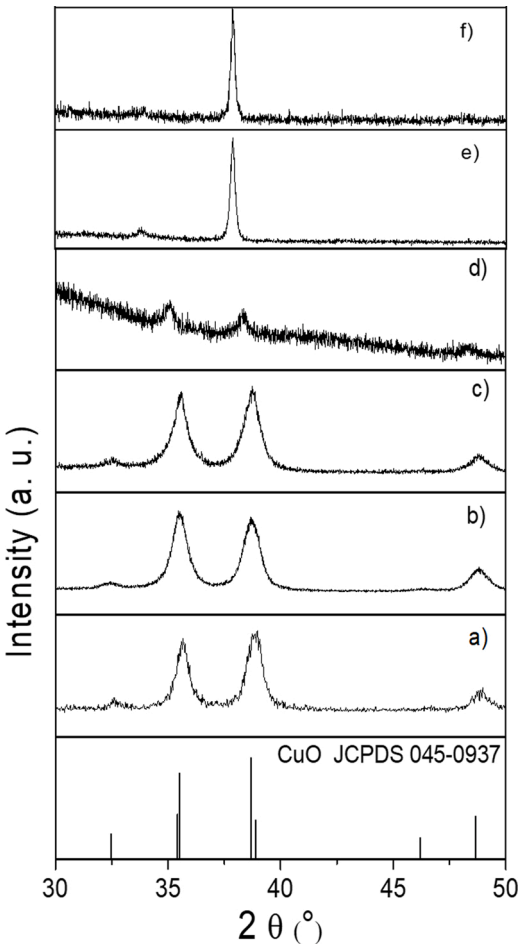

Fig. 1. XRD patterns of a) CuO P, b) CuO US, c) CuO MW, d) CuO Coat, e) FTO, and f) CuO TF.

3.2. Morphology

The morphology of the fabricated samples was investigated using SEM. Samples CuO P, CuO US and CuO MW possessed a mixture of nanorods and agglomerated nanoparticles (Fig. 2a–c). The length of the nanorods observed in the sample CuO US (~580 nm, Fig. 2b) was longer than that in CuO P (~400 nm, Fig. 2a) and CuO MW (~408 nm, Fig. 2c). Very similar observation was also obtained on sample CuO Coat, but a more homogeneous nanorods coated on the surface of the glass fiber mesh was observed (~445 nm in length, Fig. 2d). The CuO TF fabricated revealed a patchy microstructure resulted the broadening and red-shifted of the Raman spectrum in this sample (Fig. 2f).

3.3. Optical properties

The optical properties of the fabricated samples were investigated and analyzed using UV–vis spectroscopy, as shown in Fig. 3. The band gap energy of was derived using the Kubelka-Munk function from diffuse reflectance. All the fabricated samples showed a band gap of around 1.4–1.5 eV using the (Fig. 3).

3.4. Surface properties

To investigate the surface chemistry of the samples, XPS was performed (Fig. 4). The XPS survey spectra of samples CuO P, CuO US, CuO

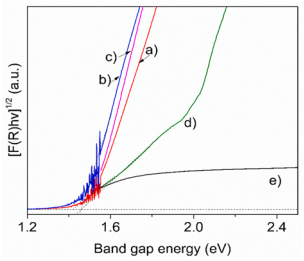

Fig. 3. Kubelka-Munk spectra of a) CuO P, b) CuO US, c) CuO MW, d) CuO Coat, and e) CuO TF.

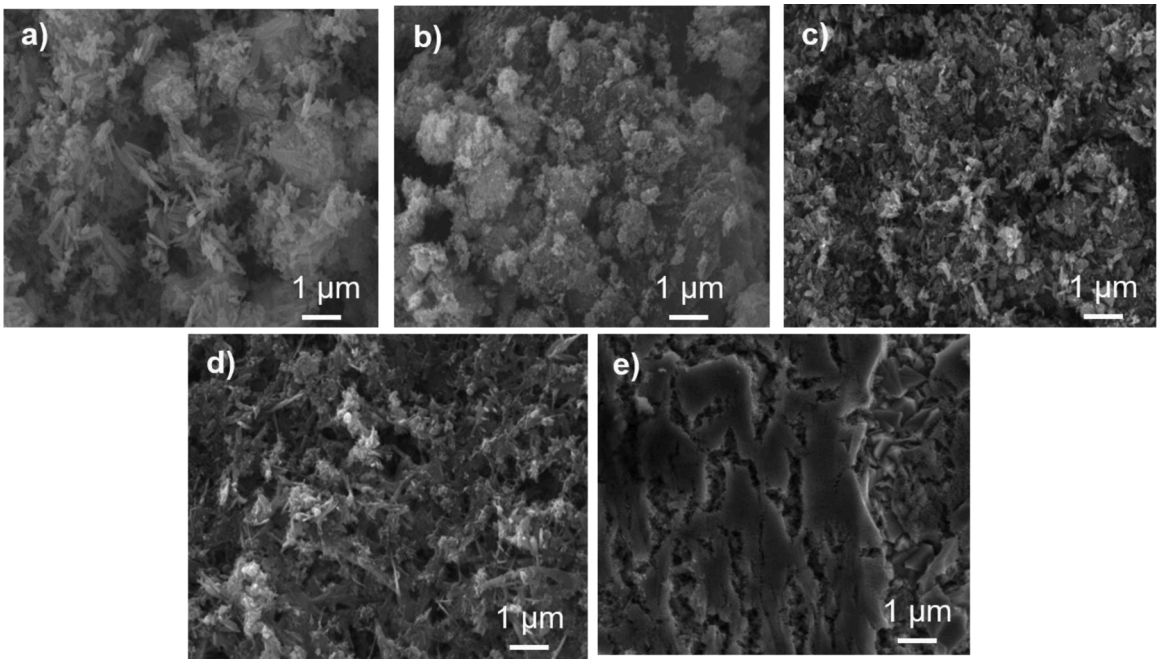

Fig. 2. SEM of the a) CuO P, b) CuO US, c) CuO MW, d) CuO Coat, and e) CuO TF.

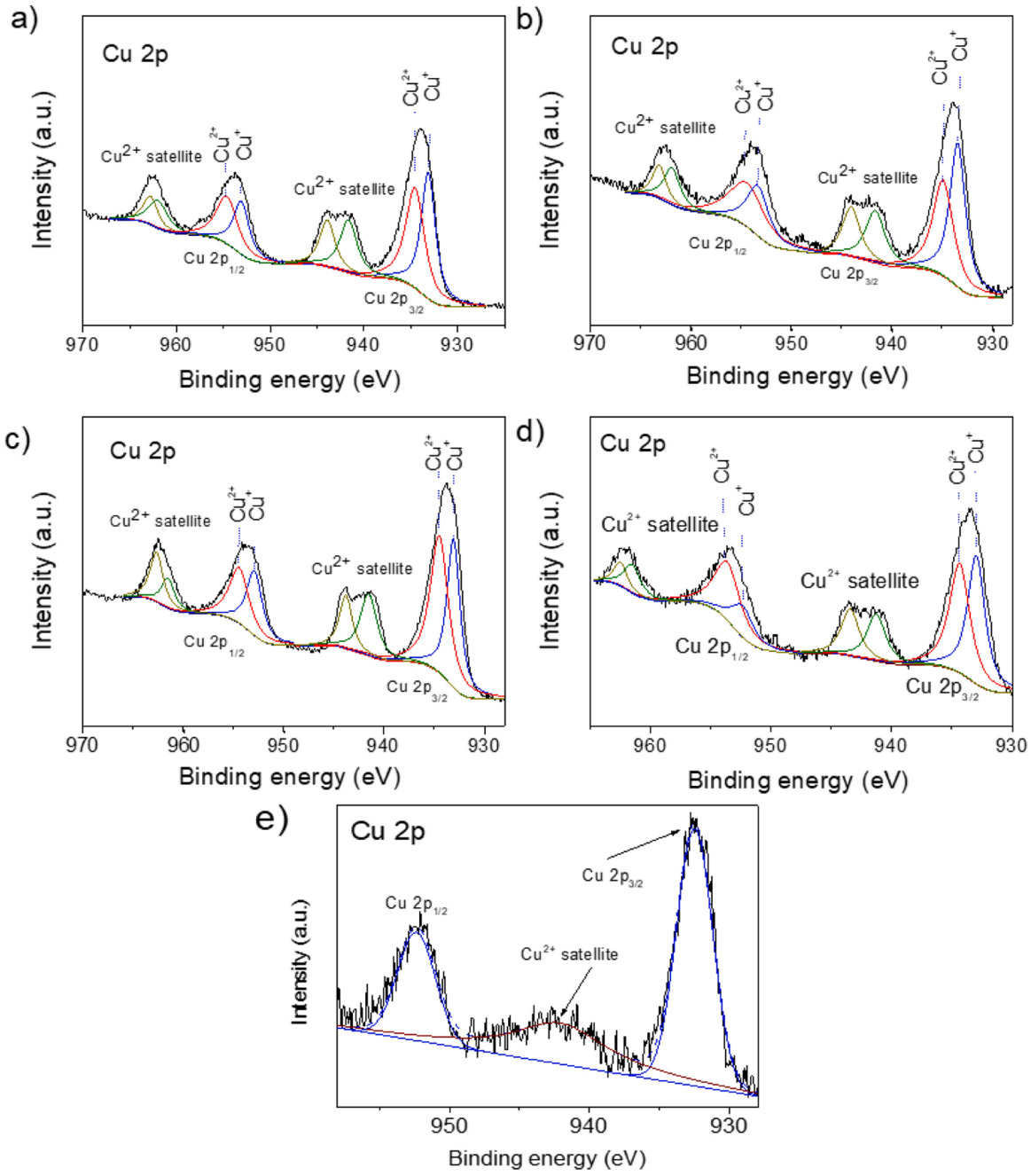

Fig. 4. XPS spectra of Cu 2p for a) CuO P, b) CuO US, c) CuO MW, d) CuO Coat, and e) CuO TF.

MW and CuO TF revealed no contamination from the precursors nor substrates, whereas CuO Coat revealed the presence of Na, which was originated from the glass fiber mesh (Figure S2).

The Cu 2p spectra of all the samples were deconvoluted into two components. Specifically, the Cu $2p_{3/2}$ (934.5 eV for CuO P and CuO MW; 934.9 eV for CuO US) and Cu $2p_{1/2}$ species (954.7 eV for CuO P and CuO US; 954.6 eV for CuO MW; Fig. 4a–c). In addition, these components were accompanied by their respective satellite peaks positioning at 961.0–963.9 eV, which are characteristic of Cu^{2+}. Furthermore, the difference between the Cu $2p_{1/2}$ and Cu $2p_{3/2}$ peaks was ~20 eV, which evidenced the oxidation state of the fabricated samples as Cu^{2+} [36,37]. The presence of Cu^{+} on the surface of the fabricated materials was revealed in the peaks centered at 933.1 and 953.1 eV for CuO P; 933.6 and 953.2 eV for CuO US; and 933.1, and 953.0 eV for CuO MW (Fig. 4a–c) [38]. Meanwhile, CuO Coat had the Cu $2p_{3/2}$ peak centered at 934.5 and 934.2 eV and Cu $2p_{1/2}$ peak located at 953.8 eV. Similarly, the difference of Cu $2p_{1/2}$ and Cu $2p_{3/2}$ in CuO Coat remained ~20 eV, confirming the fabricated CuO Coat sample contained Cu (II) (Fig. 4d). This sample also contained Cu^{+} as exhibited in the peak positioned at 933.1 eV (Fig. 4d) but absent in CuO TF (Fig. 4e). CuO TF exhibited only the Cu $2p_{3/2}$, Cu $2p_{1/2}$ and Cu satellite peaks at 932.7, 952.4 and 962.1 eV, respectively (Fig. 4e), confirming the presence of CuO on the thin films.

The high-resolution of O 1s spectrum were deconvoluted into four components (Figure S3). The peak centered at 529.5–529.9, were attributed to the O^{2-} in O_L-CuO [39,40]. Meanwhile, the presence of peak centered at 531.1 (*i.e.*, samples CuO US, and CuO Coat) and 530.2 eV (*i.e.*, sample CuO P and CuO MW) was attributed to V_{Os} [41–43], evidencing the presence of V_{Os} in these samples. Other peaks located at 531.9–532.3 eV were attributed to the oxygen adsorbed on the surface

with low coordination [44,45].

High resolution XPS spectra at low binding energy region were also collected to investigate the position of the valence band. The valence band of the fabricated samples was positioned at ~1.6 eV, indicating the CuO-based sample possessed sufficient potential to reduce CO_2 to CH_4 (Scheme 1) [46].

3.5. Photocatalytic activity

The fabricated CuO samples in different conformations were evaluated for the photocatalytic reduction of CO_2 under the light irradiation (300−600 nm) and the quantity of the gaseous products produced (CO and CH_4) were monitored (Table 1). In general, CH_4 was the main product produced by all the fabricated CuO samples in the photocatalytic reduction of CO_2, whereas CO was generated in very low quantities.

The CH_4 production of the powder samples declined in the order of CuO MW (2.6 μmol g_{cat}^{-1} h^{-1}) > CuO US (1.5 μmol g_{cat}^{-1} h^{-1}) > CuO P (1.0 μmol g_{cat}^{-1} h^{-1}). This could be due to the homogeneity of the particles of the samples fabricated using the microwave-hydrothermal approach. The action spectra of the CO_2 photoreduction for the fabricated samples is shown in Figure S4.

Regarding to the photocatalytic activity of the immobilized photocatalysts, sample CuO TF, which contained only CuO, exhibited 100 % selectivity towards CH_4, producing 12.7 μmol g_{cat}^{-1} h^{-1} under visible light irradiation. Sample CuO Coat showed the highest production of CH_4 (56.3 μmol g_{cat}^{-1} h^{-1}), which was approximately 18 times higher than that of CuO MW (*i.e.*, highest among the fabricated powdered samples). The superior performance of CuO Coat (ϕCH_4 = 0.882) was due to the reduction of agglomeration and the presence of Na_2O originated from the mesh substrate as shown in the FTIR (Fig. 5) [47,48]. The presence of Na_2O had significantly enhance the CO_2 adsorption (further discussed in the next paragraph). The CuO Coat, which has the highest CH_4 production was implemented for cycling test (Figure S5). The sample was tested for 3 runs and did not show significant reduction in CH_4 production.

The mechanistic study of the best performing sample (*i.e.*, CuO Coat) was conducted using FTIR in the presence of CO_2 (Fig. 5). A series of

Table 1
Average products obtained in 4 h from CO_2 photoreduction using different configurations of photocatalyst.

Sample name	CH_4 (μmol g_{cat}^{-1} h^{-1})
CuO P	1.0
CuO US	1.5
CuO MW	2.6
CuO Coat	56.3
CuO TF	12.7

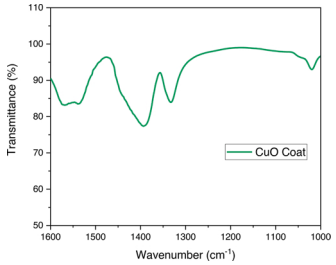

Fig. 5. FTIR pattern of CuO Coat upon the exposure of CO_2.

bands at 1560 and 1410 cm^{-1}, which could be associated with C − O stretching and symmetry O − C − O vibrational modes, was assigned to monodentate species (linear coordination or carbon coordination) [49,50]. In addition, C − O stretching and symmetry O − C − O vibrational modes, which were shown at 1340 and 1020 cm^{-1} corresponded to the bidentate carbonate [51]. Based on the results obtained, the CO_2 adsorption and conversion mechanisms in CuO Coat sample was proposed and shown in Scheme 2. Briefly, the O and Cu on the surface of CuO Coat acts as a Lewis base site – an active site for CO_2 adsorption and conversion. Then, electrons were transferred to the C and/or O of the CO_2 molecules resulted in the formation of monodentate and bidentate configurations at the surface of CuO Coat. The hole-electron pairs, which were generated upon light irradiation, traveled to the surface of the photocatalyst and underwent the subsequent oxidation-reduction reactions. CO_2 was reduced to CH_4 and H_2O was oxidized to O_2 and H^+.

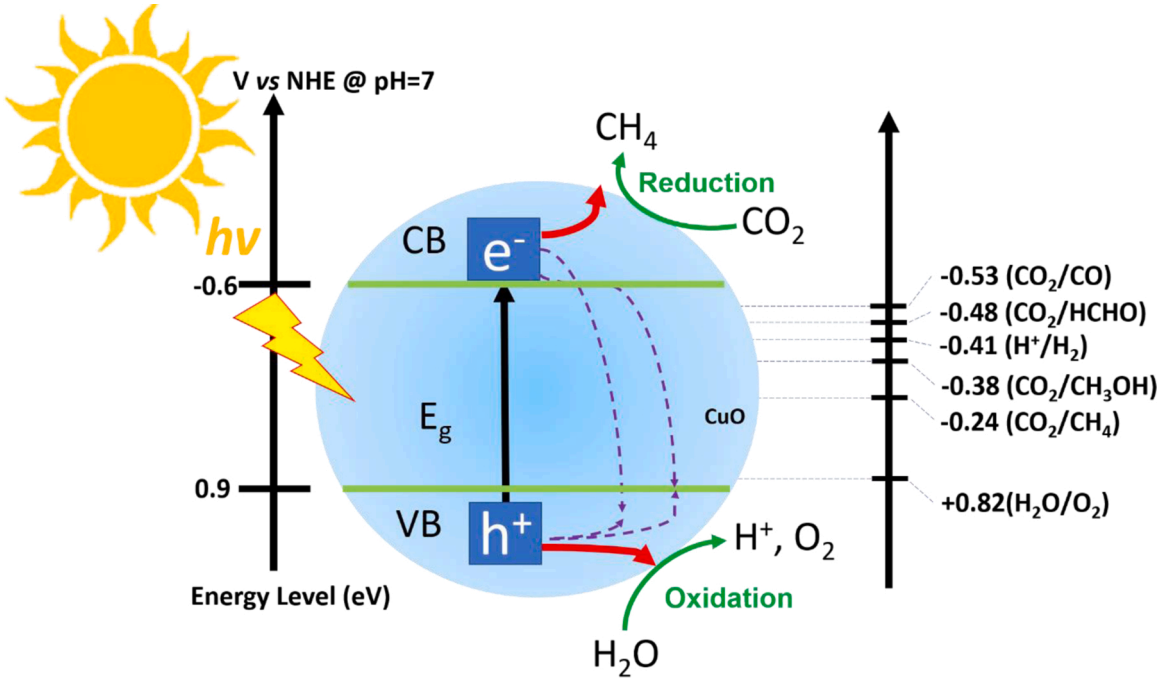

Scheme 1. Schematic illustration of CO_2 photocatalytic reduction with H_2O under using CuO under visible light irradiation.

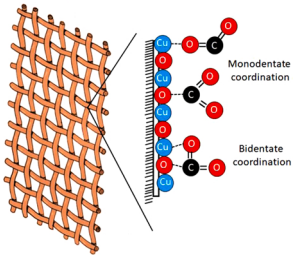

Scheme 2. Schematic illustration of CO_2 adsorption and conversion on the surface of CuO Coat sample.

The CuO coat was analyzed with *operando* DRIFTS to confirm the formation of carbonate species (Figure S6). The coating presented a strong adsorption band at 2348 cm^{-1}, which assigns to CO_2 physisorbed in the surface of the coating, when CO_2 was fed into the reactor and put in contact with the photocatalyst at 24 °C in the dark. On the other hand, the bands at around 1620, 1420 and 1296 cm^{-1} were assigned to the asymmetric CO_3 stretching vibration [$\nu_{as}(CO_3)$], symmetric CO_3 stretching vibration [$\nu_s(CO_3)$] and O—H deformation vibration [δ(O-H)] of monodentate bicarbonate species ($m-HCO_3^{2-}$), respectively, were observed upon CO_2 interaction with the coating in the dark [3,52]. When the coating was irradiated with UV–vis light, the intensity of these bands lowered. The bands at around 1540 and 1384 cm^{-1} corresponds to the [$\nu_{as}(CO_2)$] and [$\nu_s(CO_2)$] of the bidendate formate species ($b-HCO_2^{2-}$). [53] These results suggested that the CO_2 molecules adsorbed on the surface of CuO coat were mainly $m-HCO_3^{2-}$ and converted to $b-HCO_2^{2-}$ through the reaction with OH- on the surface or OVs CuO coating. When the reaction temperature increased to 40 °C (to emulate the reaction conditions), the bands of $m-HCO_3^{2-}$ continued to decrease, whereas $b-HCO_2^{2-}$ increased steadily. In other words, adsorption of CO_2 and conversion of $m-HCO_3^{2-}$ to $b-HCO_2^{2-}$ were enhanced at elevated temperature, which could favor the formation of CH_4. Therefore, *operando* DRIFT results suggested that the mechanism for the photocatalytic CO_2 reduction route of CuO coat was through the carbene pathway [48,53].

3.6. Simulation study

To gain insight in the coupled physical/chemical processes, parametric simulations (CO_2 gas flow, humidity, and light intensity) were performed. The simulated photocatalytic activity values obtained from the constructed models using COMSOL multiphysics software matched well with the experimental results as shown in Fig. 6. The simulation revealed that the flow rate of CO_2 had almost no effect on the photoreduction reaction rate (Fig. 6a). However, the simulated CO_2 utilization rate dropped rapidly with increasing CO_2 flow rates for values up to 5 SCCM (Fig. 6d). Further increasing the CO_2 flow rates would eventually lead to zero CO_2 utilization rate. This phenomenon was expected due to the reduction of contact time between the gas (CO_2) and solid (photocatalyst) phases at high flow rate as reported in other work [54].

Increasing the water content exhibited a remarkable improvement in the reaction rate, (Fig. 6b) and CO_2 utilization rate (Fig. 6e), especially for sample CuO MW. Hence, the simulated results indicated that the water content for the CO_2 photoreduction was far below the saturation point. Further increasing the water content will promote the photocatalytic reduction of CO_2.

The light intensity applied to stimulate the CO_2 photoreduction reaction strongly depended on the properties of the photocatalyst, including microstructure, surface area, *etc.* For instance, sample CuO Coat with rod-shape nanostructure exhibited the highest reaction rate and CO_2 utilization rate; whereas samples CuO TF and CuO MW with patchy-structures and agglomeration revealed a much lower performance (Fig. 6c and f).

4. Conclusions

CuO photocatalysts with different configurations (powder, thin film, and coatings on glass fiber mesh) were fabricated and their CO_2 photoreduction activity was investigated. Sample CuO Coat with highly dispersed nanorod structure coated on the glass fiber mesh showed the highest CH_4 production from CO_2 (56.3 μmol g_{cat}^{-1} h^{-1}), which was approximately 18 times higher than the powder sample synthesized using the similar method (CuO MW). Combining the experimental and

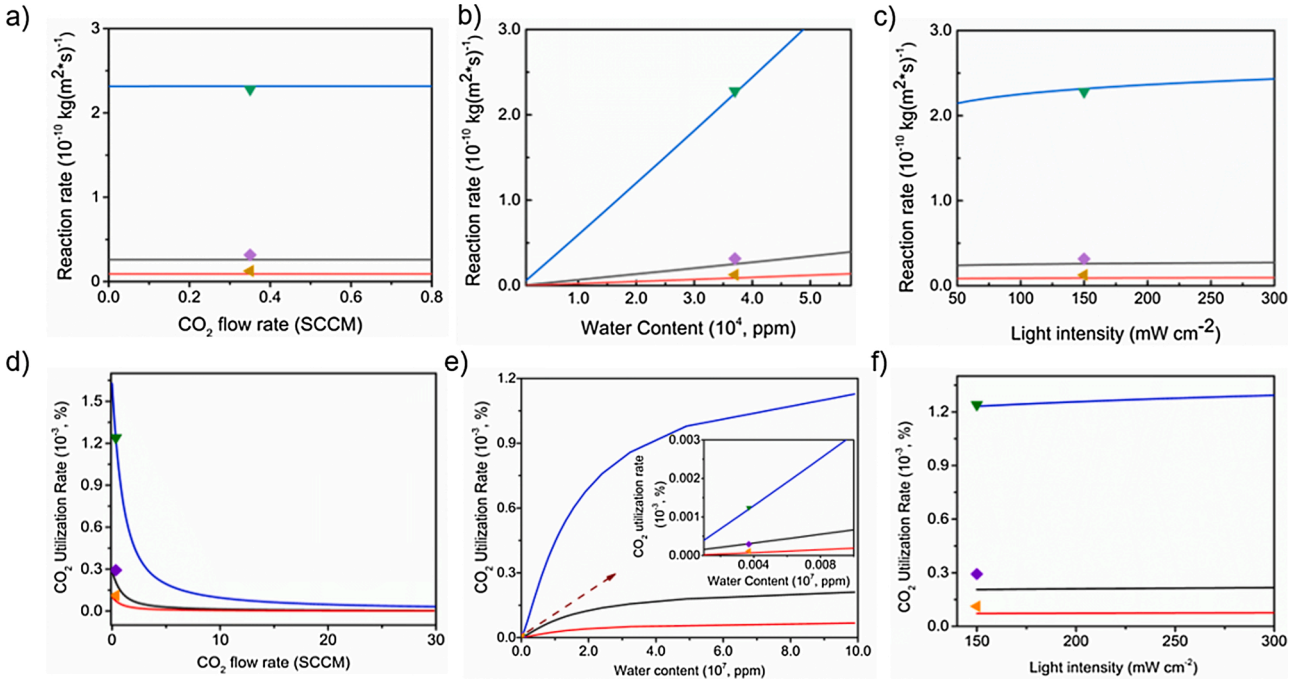

Fig. 6. Simulated patterns (lines: black- CuO TF, orange- CuO MW, blue- CuO Coat) and experimental results (purple ◆: CuO TF, orange◥: CuO TF, green▼: CuO TF) of the CO_2 photoreduction reaction rate and CO_2 utilization rate influenced by the (a and d) CO_2 flow rate, (b and e) water content, (c and f) light intensity.

simulated results, the use of highly dispersive nanostructured photocatalyst operated at ~6.0×10^7 ppm and ≤2 SCCM of water content and CO_2 flow rate, respectively, could achieve the maximum yield of CO_2 photoreduction at 40 °C.

Author statement

Manuel Alejandro Ávila-López: Methodology, Data curation, Writing- Original draft preparation.

Stelios Gavrielides: Methodology, Data curation, Writing- Original draft preparation.

XiaoJiao Luo: Investigation, Data curation, Software, Validation.

Abah Ezra Ojoajogwu: Methodology.

Jeannie Z. Y. Tan: Conceptualization, Methodology, Writing-Reviewing and Editing.

E. Luévano-Hipólitoc: Supervision.

Leticia M. Torres-Martíneza: Supervision.

M. Mercedes Maroto-Valer: Supervision.

Author contributions

The manuscript was written through contributions of all authors. All authors have given approval to the final version of the manuscript.

Funding sources

The work is financially supported by the Engineering and Physical Sciences Research Council (EP/K021796/1) and CONACYT through the projects Cátedras CONACYT 1060 and CONACYT-FC-1725.

Declaration of Competing Interest

There are no conflicts to declare.

Acknowledgements

The authors thank the financial support provided by the Engineering and Physical Sciences Research Council (EP/K021796/1) and the Research Centre for Carbon Solutions (RCCS) at Heriot-Watt University, United Kingdom; and the financial support from Cátedras CONACYT 1060 and CONACYT-FC-1725, in Mexico. Manuel Alejandro Ávila López wants to thank CONACYT for the PhD scholarship, number 70725. Stelios Gavrielides thanks CRITICAT for the PhD scholarship. XPS data collection was performed at the EPSRC National Facility for XPS ('HarwellXPS'), operated by Cardiff University and UCL, under contract No. PR16195.

Appendix A. Supplementary data

Supplementary material related to this article can be found, in the online version, at doi:https://doi.org/10.1016/j.jcou.2021.101588.

References

[1] Y. Wang, L. Zhao, A. Otto, M. Robinius, D. Stolten, A review of post-combustion CO2 capture technologies from coal-fired power plants, Energy Procedia 114 (2017) 650–665, https://doi.org/10.1016/j.egypro.2017.03.1209.

[2] D.Y.C. Leung, G. Caramanna, M.M. Maroto-Valer, An overview of current status of carbon dioxide capture and storage technologies, Renewable Sustainable Energy Rev. 39 (2014) 426–443, https://doi.org/10.1016/j.rser.2014.07.093.

[3] L. Liu, C. Zhao, J. Xu, Y. Li, Integrated CO2 capture and photocatalytic conversion by a hybrid adsorbent/photocatalyst material, Appl. Catal. B Environ. 179 (2015) 489–499, https://doi.org/10.1016/j.apcatb.2015.06.006.

[4] A. Crake, K.C. Christoforidis, A. Kafizas, S. Zafeiratos, C. Petit, CO2 capture and photocatalytic reduction using bifunctional TiO2/MOF nanocomposites under UV–vis irradiation, Appl. Catal. B Environ. 210 (2017) 131–140, https://doi.org/10.1016/j.apcatb.2017.03.039.

[5] M. Flores-Flores, E. Luévano-Hipólito, L.M.T. Martínez, G. Morales-Mendoza, R. Gómez, Photocatalytic CO2 conversion by MgAl layered double hydroxides: effect of Mg2+ precursor and microwave irradiation time, J. Photochem. Photobiol. A: Chem. 363 (2018) 68–73, https://doi.org/10.1016/j.jphotochem.2018.05.033.

[6] A. Li, T. Wang, X. Chang, Z.J. Zhao, C. Li, Z. Huang, P. Yang, G. Zhou, J. Gong, Tunable syngas production from photocatalytic CO2 reduction with mitigated charge recombination driven by spatially separated cocatalysts, Chem. Sci. 9 (2018) 5334–5340, https://doi.org/10.1039/c8sc01812j.

[7] G. Qin, Y. Zhang, X. Ke, X. Tong, Z. Sun, M. Liang, S. Xue, Photocatalytic reduction of carbon dioxide to formic acid, formaldehyde, and methanol using dye-sensitized TiO2 film, Appl. Catal. B Environ. 129 (2013) 59–605, https://doi.org/10.1016/j.apcatb.2012.10.012.

[8] J.Z.Y. Tan, Y. Fernández, D. Liu, M. Maroto-Valer, J. Bian, X. Zhang, Photoreduction of CO2 using copper-decorated TiO2 nanorod films with localized surface plasmon behavior, Chem. Phys. Lett. 531 (2012) 149–154, https://doi.org/10.1016/j.cplett.2012.02.016.

[9] O. Ola, M.M. Maroto-valer, Copper based TiO2 honeycomb monoliths for CO2 photoreduction, Catal. Sci. Technol. 4 (2014) 1631–1637, https://doi.org/10.1039/c3cy00991b.

[10] W.A. Thompson, C. Perier, M.M. Maroto-Valer, Systematic study of sol-gel parameters on TiO2 coating for CO2 photoreduction, Appl. Catal. B Environ. 238 (2018) 136–146, https://doi.org/10.1016/j.apcatb.2018.07.018.

[11] D. Liu, Y. Fernández, O. Ola, S. Mackintosh, M. Maroto-Valer, C.M.A. Parlett, A. F. Lee, J.C.S. Wu, On the impact of Cu dispersion on CO2 photoreduction over Cu/TiO2, Catal. Commun. 25 (2012) 78–82, https://doi.org/10.1016/j.catcom.2012.03.025.

[12] Y. Chiang, R. Juang, Journal of the Taiwan Institute of Chemical Engineers Surface modifications of carbonaceous materials for carbon dioxide adsorption : a review, J. Taiwan Inst. Chem. Eng. 71 (2017) 214–234, https://doi.org/10.1016/j.jtice.2016.12.014.

[13] Q. Wang, J. Luo, Z. Zhong, A. Borgna, CO2 capture by solid adsorbents and their applications: current status and new trends, Energy Environ. Sci. 4 (2011) 42–55, https://doi.org/10.1039/C0EE00064G.

[14] S. Sun, Recent advances in hybrid Cu2O-based heterogeneous nanostructures, Nanoscale 7 (2015) 10850–10882, https://doi.org/10.1039/c5nr02178b.

[15] M. Janczarek, E. Kowalska, On the origin of enhanced photocatalytic activity of copper-modified titania in the oxidative, Catal. MDPI. 7 (2017) 1–26, https://doi.org/10.3390/catal7110317.

[16] W.N.R.W. Isahak, Z.A.C. Ramli, M.W. Ismail, K. Ismail, R.M. Yusop, M.W. M. Hisham, M.A. Yarmo, Adsorption-desorption of CO2 on different type of copper oxides surfaces: physical and chemical attractions studies, J. CO2 Util. 2 (2013) 8–15, https://doi.org/10.1016/j.jcou.2013.06.002.

[17] B.J. Kim, K.S. Cho, S.J. Park, Copper oxide-decorated porous carbons for carbon dioxide adsorption behaviors, J. Colloid Interface Sci. 342 (2010) 575–578, https://doi.org/10.1016/j.jcis.2009.10.045.

[18] J.-C. Wang, L. Zhang, W. Fang, J. Ren, Y.-Y. Li, H. Yao, J. Wang, Z. Li, Enhanced photoreduction CO 2 activity over direct Z-Scheme α-Fe 2 O 3 /Cu 2 O Heterostructures under visible light irradiation, ACS Appl. Mater. Interfaces 7 (2015) 8631–8639, https://doi.org/10.1021/acsami.5b00822.

[19] S. Il In, D.D. Vaughn, R.E. Schaak, Hybrid CuO-TiO2-xNx hollow nanocubes for photocatalytic conversion of CO2 into methane under solar irradiation, Angew. Chemie - Int. Ed. 51 (2012) 3915–3918, https://doi.org/10.1002/anie.201108936.

[20] N. Jantarasorn, O. Mekasuwandumrong, P. Kelly, P. Praserthdam, Reactive magnetron sputter deposition of copper on TiO2 support for photoreduction of CO2 to CH4, IOP Conf. Ser. Mater. Sci. Eng. 559 (2019) 012017, https://doi.org/10.1088/1757-899X/559/1/012017.

[21] Z. Xiong, Z. Lei, C.-C. Kuang, X. Chen, B. Gong, Y. Zhao, J. Zhang, C. Zheng, J.C. S. Wu, Selective photocatalytic reduction of CO2 into CH4 over Pt-Cu2O TiO2 nanocrystals: The interaction between Pt and Cu2O cocatalysts, Appl. Catal. B Environ. 202 (2017) 695–703, https://doi.org/10.1016/j.apcatb.2016.10.001.

[22] A.E. Nogueira, J.A. Oliveira, G.T.S.T. da Silva, C. Ribeiro, Insights into the role of CuO in the CO2 photoreduction process, Sci. Rep. 9 (2019) 1316, https://doi.org/10.1038/s41598-018-36683-8.

[23] M.L. Ovcharov, A.M. Mishura, N.D. Shcherban, S.M. Filonenko, V.M. Granchak, Photocatalytic reduction of CO2 using nanostructured Cu2O with foam-like structure, Sol. Energy 139 (2016) 452–457, https://doi.org/10.1016/j.solener.2016.10.010.

[24] T. Arai, S. Sato, T. Morikawa, A monolithic device for CO2 photoreduction to generate liquid organic substances in a single-compartment reactor, Energy Environ. Sci. 8 (2015) 1998–2002, https://doi.org/10.1039/C5EE01314C.

[25] M. Tahir, N.S. Amin, Photocatalytic CO2 reduction with H2O vapors using montmorillonite/TiO2 supported microchannel monolith photoreactor, Chem. Eng. J. 230 (2013) 314–327, https://doi.org/10.1016/j.cej.2013.06.055.

[26] M.A. Ávila-López, E. Luévano-Hipólito, L.M. Torres-Martínez, CO2 adsorption and its visible-light-driven reduction using CuO synthesized by an eco-friendly sonochemical method, J. Photochem. Photobiol. A: Chem. 382 (2019), https://doi.org/10.1016/j.jphotochem.2019.111933.

[27] W.A. Thompson, A. Olivo, D. Zanardo, G. Cruciani, F. Menegazzo, M. Signoretto, M.M. Maroto-valer, Systematic study of TiO2/ZnO mixed metal oxides for CO2 photoreduction, R. Soc. Chem. RSC ADV. 9 (2019) 21660–21666, https://doi.org/10.1039/c9ra03435h.

[28] I.R. Lewis, H.G.M. Eduards, Handbook of Raman Spectroscopy, CRC Press, New York, USA, 2001. Year 2001.

[29] S. Guha, D. Peebles, J. Terence Wieting, Raman and infrared studies of cupric oxide, Bull. Mater. Sci. 14 (1991) 539–543, https://doi.org/10.1007/BF02744682.

[30] M. Rashad, M. Rüsing, G. Berth, K. Lischka, A. Pawlis, CuO and Co3O4 nanoparticles: synthesis, characterizations, and raman spectroscopy, J. Nanomater. 2013 (2013) 1–6, https://doi.org/10.1155/2013/714853.
[31] H.F. Goldstein, D. Kim, P.Y. Yu, L.C. Bourne, J.-P. Chaminade, L. Nganga, Raman study of CuO single crystals, Phys. Rev. B 41 (1990) 7193–7194.
[32] S. Chakraborty, A. Das, M.R. Begum, S. Dhara, A.K. Tyagi, A.B. Garg, R. Mittal, R. Mukhopadhyay, Vibrational properties of CuO nanoparticles synthesized By hydrothermal technique, AIP Conf. Proc. (2011) 841–842, https://doi.org/10.1063/1.3606120.
[33] P.E. Timchenko, E.V. Timchenko, L.T. Volova, O.O. Frolov, Chemometric analysis of the Raman spectra for determination of the composition of bones with different porosity, J. Phys. Conf. Ser. 1135 (2018) 012065, https://doi.org/10.1088/1742-6596/1135/1/012065.
[34] G. Socrates, Infrared and Raman Characteristic Group Frequencies, 3rd edit, Wiley, 2001, https://doi.org/10.1002/jrs.1238.
[36] D. He, S. Xing, B. Sun, H. Cai, H. Suo, C. Zhao, Design and construction of three-dimensional flower-like CuO hierarchical nanostructures on copper foam for high performance supercapacitor, Electrochim. Acta 210 (2016) 639–645, https://doi.org/10.1016/j.electacta.2016.05.196.
[37] L. Zhu, H. Li, Z. Liu, P. Xia, Y. Xie, D. Xiong, Synthesis of the 0D/3D CuO/ZnO heterojunction with enhanced photocatalytic activity, Phys. Chem. C. (2018), https://doi.org/10.1021/acs.jpcc.8b01933.
[38] J. Park, K. Lim, R.D. Ramsier, Y.-C. Kang, Spectroscopic and morphological investigation of copper oxide thin films prepared by magnetron sputtering at various oxygen ratios, Bull. Korean Chem. Soc. 32 (2011) 3395–3399, https://doi.org/10.5012/bkcs.2011.32.9.3395.
[39] Q. Yang, P.X. Yan, J.B. Chang, J.J. Feng, G.H. Yue, Growth of bicrystal CuO microsheets from aqueous solution, Phys. Lett. Sect. A Gen. At. Solid State Phys. 361 (2007) 493–496, https://doi.org/10.1016/j.physleta.2006.07.056.
[40] Y. Min, T. Wang, Y. Chen, Microwave-assistant synthesis of ordered CuO microstructures on Cu substrate, Appl. Surf. Sci. 257 (2010) 132–137, https://doi.org/10.1016/j.apsusc.2010.06.049.
[41] W. Li, R. Liang, A. Hu, Z. Huang, Y.N. Zhou, Generation of oxygen vacancies in visible light activated one-dimensional iodine TiO2 photocatalysts, RSC Adv. 4 (2014) 36959–36966, https://doi.org/10.1039/c4ra04768k.
[42] H. Yu, J. Li, Y. Zhang, S. Yang, K. Han, F. Dong, T. Ma, H. Huang, Three-in-One Oxygen Vacancies: Whole Visible-Spectrum Absorption, Efficient Charge Separation, and Surface Site Activation for Robust CO2 Photoreduction, Angew. Chemie - Int. Ed. 58 (2019) 3880–3884, https://doi.org/10.1002/anie.201813967.
[43] Z.P. Nie, D.K. Ma, G.Y. Fang, W. Chen, S.M. Huang, Concave Bi2WO6 nanoplates with oxygen vacancies achieving enhanced electrocatalytic oxygen evolution in near-neutral water, J. Mater. Chem. A 4 (2016) 2438–2444, https://doi.org/10.1039/c5ta09536k.
[44] E. Desimoni, B. Brunetti, X-ray photoelectron spectroscopic characterization of chemically modified electrodes used as chemical sensors and biosensors: a review, Chemosensors 3 (2015) 70–117, https://doi.org/10.3390/chemosensors3020070.
[45] S. Jaiswar, K.D. Mandal, Evidence of enhanced oxygen vacancy defects inducing ferromagnetism in multiferroic CaMn7O12 manganite with sintering time, J. Phys. Chem. C. 121 (2017) 19586–19601, https://doi.org/10.1021/acs.jpcc.7b05415.
[46] S. Gavrielides, J.Z.Y. Tan, E.S. Fernandez, M.M. Maroto-Valer, Photo-generation of cyclic carbonates using hyper-branched Ru–TiO2, Faraday Discuss. 215 (2019) 407–421, https://doi.org/10.1039/C8FD00181B.
[47] L. Proaño, E. Tello, M.A. Arellano-Trevino, S. Wang, R.J. Farrauto, M. Cobo, In-situ DRIFTS study of two-step CO2 capture and catalytic methanation over Ru,"Na2O"/Al2O3 Dual Functional Material, Appl. Surf. Sci. 479 (2019) 25–30, https://doi.org/10.1016/j.apsusc.2019.01.281.
[48] M.A. Ávila-López, E. Luévano-Hipólito, L.M. Torres-Martínez, CuO coatings on glass fibers: a hybrid material for CO2 adsorption and photocatalytic reduction to solar fuels, J. Mater. Sci. Mater. Electron. 31 (2020) 13957–13969, https://doi.org/10.1007/s10854-020-03955-x.
[49] H. Du, C.T. Williams, A.D. Ebner, J.A. Ritter, In situ FTIR spectroscopic analysis of carbonate transformations during adsorption and desorption of CO2 in K-Promoted HTlc, Chem. Mater. 22 (2010) 3519–3526, https://doi.org/10.1021/cm100703e.
[50] Y. Liu, Y. Yang, Q. Sun, Z. Wang, B. Huang, Y. Dai, X. Qin, X. Zhang, Chemical adsorption enhanced CO 2 capture and photoreduction over a copper porphyrin based metal organic framework, ACS Appl. Mater. Interfaces 5 (2013) 7654–7658, https://doi.org/10.1021/am4019675.
[51] A. Hakim, T.S. Marliza, N.M. Abu Tahari, R.W.N. Wan Isahak, R.M. Yusop, W. M. Mohamed Hisham, A.M. Yarmo, Studies on CO 2 adsorption and desorption properties from various types of Iron oxides (FeO, Fe 2 O 3, and Fe 3 O 4), Ind. Eng. Chem. Res. 55 (2016) 7888–7897, https://doi.org/10.1021/acs.iecr.5b04091.
[52] Y. Kato, M. Yamamoto, M. Akatsuka, R. Ito, A. Ozawa, Y. Kawaguchi, T. Tanabe, T. Yoshida, Study on carbon dioxide reduction with water over metal oxide photocatalysts, Surf. Interface Anal. 51 (2019) 40–45, https://doi.org/10.1002/sia.6542.
[53] S.N. Habisreutinger, L. Schmidt-Mende, J.K. Stolarczyk, Photocatalytic reduction of CO 2 on TiO 2 and other semiconductors, Angew. Chem. Int. Ed. 52 (2013) 7372–7408, https://doi.org/10.1002/anie.201207199.
[54] A. Dey, A. Aroonwilas, CO2 absorption into MEA-AMP blend: mass transfer and absorber height index, Energy Procedia 1 (2009) 211–215, https://doi.org/10.1016/j.egypro.2009.01.030.